Rare Metal Materials and Engineering
Volume 54, Issue 10, October 2025
Available online at www.rmme.ac.cn

Science Press

Cite this article as: Han Chengxu, Liu Yanming, Wang Xin, et al. Effect of Si Content on In-situ Formation Mechanism of Hf-Ta-Si Coating on Ta12W Alloy Surface[J]. Rare Metal Materials and Engineering, 2025, 54(10): 2509-2524. DOI: https://doi.org/10.12442/j.issn.1002-185X.20250303.

ARTICLE

Effect of Si Content on In-situ Formation Mechanism of Hf-Ta-Si Coating on Ta12W Alloy Surface

Han Chengxu[1,2], Liu Yanming[1], Wang Xin[2], Yang Tao[2], Yan Peng[2]

[1] College of Materials Science and Engineering, Xi'an Shiyou University, Xi'an 710065, China; [2] Northwest Institute for Nonferrous Metal Research, Xi'an 710016, China

Abstract: Using the slurry reaction sintering process to prepare Hf-Ta-Si composite coating on Ta12W alloy surface, the effect of Si content on the in-situ formation mechanism of the Hf-Ta-Si coating was investigated. Results show that 30Hf:70Si coatings exhibit inferior surface uniformity with some pores. The upper part of the sample displays a four-layer gradient structure: the outermost layer is primarily composed of HfSi and HfC, the middle layer consists of (Ta, Hf)$_5$Si$_3$ solid solution, the lower main-layer consists of TaSi$_2$, and the coating/substrate interface layer is Ta$_5$Si$_3$. However, the flow of molten Si under gravity leads to Si-enrichment on the lower part of the coating. After optimizing the Hf:Si ratio to 40:60, the gradient differences in elemental distribution on the coating surface decrease. The surface layer is dominated by HfSi/HfC, but the precipitation of HfC becomes more uniform. The continuity of the (Ta, Hf)$_5$Si$_3$ solid solution in middle layer is enhanced, whereas the lower layer and the interface transition layer remain unchanged. Overall, a denser multi-layer gradient structure is formed with improved surface uniformity. Additionally, the acid-alcohol resin in the organic solvent suffers high-temperature pyrolysis and in-situ reacts with Hf to generate the ultra-high-temperature ceramic HfC. This phenomenon is expected to enhance the oxidation resistance and high-temperature stability of coating.

Key words: Ta-based alloy; Hf-Ta-Si coating; in-situ formation mechanism; HfC; gradient structure

1 Introduction

Tantalum and its alloys are extensively utilized in high-temperature environments owing to their high density, excellent cold workability, high thermal conductivity, and strong corrosion resistance. Among them, tantalum-tungsten alloys with superior high-temperature mechanical properties have emerged as ideal candidates for hot-end components, such as hypersonic vehicles, rocket engine nozzles, and missile nose cones[1]. However, tantalum-tungsten alloys undergo rapid oxidation at around 500 °C, producing an oxide layer of Ta_2O_5 with a high Pilling-Bedworth ratio (PBR, the molar volume ratio of a metal oxide to the metal consumed in forming the oxide) of approximately 2.47[2]. The high PBR value leads to significant stress during the growth process of the oxide film, affecting the bonding strength between the oxide film and the tantalum alloy matrix, which in turn easily causes the formation of defects, such as cracks. Furthermore, the porous nature of the Ta_2O_5 oxide film further weakens the structural integrity of the oxide film. Therefore, in oxygen-rich environments above 500 °C, the Ta_2O_5 oxide film on the surface of tantalum alloys suffers severe cracking and spalling due to the dual effects of stress and pores, leading to easy contact between oxygen and tantalum alloy matrix. This phenomenon accelerates the oxidation reaction, ultimately leading to rapid oxidative failure of the tantalum alloy in such environments[3].

Currently, applying high-temperature protective coatings on tantalum-based alloys has become an effective approach to improve their high-temperature oxidation resistance[2,4–8]. Surface coating technique can improve the oxidation resistance of refractory alloys without compromising the

Received date: May 29, 2025
Foundation item: National Natural Science Foundation of China (52071274); Natural Science Foundation of Shaanxi Province of China (2025JC-YBMS-466); Key Research and Development Projects of Shaanxi Province (2023-YBGY-442); Science and Technology Nova Project-Innovative Talent Promotion Program of Shaanxi Province (2020KJXX-062)
Corresponding author: Wang Xin, Ph. D., Professor, Northwest Institute for Nonferrous Metal Research, Xi'an 710016, P. R. China, E-mail: wangx@alum.imr.ac.cn; Liu Yanming, Ph. D., Associate Professor, College of Materials Science and Engineering, Xi'an Shiyou University, Xi'an 710065, P. R. China, E-mail: ymliu10s@alum.imr.ac.cn

mechanical properties of the substrate. Various methods are used to prepare oxidation-resistant coatings on refractory metal alloys, such as slurry sintering, halide-activated pack cementation (HAPC)[9], spark plasma sintering (SPS)[9], and hot dip siliconizing (HDS)[10–13]. The slurry sintering process is characterized by simplicity, cost-effectiveness, material adaptability, high bonding strength, and applicability to complex-shaped substrates, enabling large-scale low-cost production for industrial use. This technique allows for the in-situ formation of multiphase composite coatings in a single step, minimizing the cracks and pores. The multilayer gradient structure alleviates stress concentration and effectively accommodates thermal mismatches. A diffusion layer forms between the coating and the substrate through metallurgical bonding, significantly improving adhesion and mitigating the detachment issue of traditional coatings. Furthermore, Liu[14] and Lin[15] et al reported that the in-situ formation can enhance the high-temperature strength-ductility synergy, yield strength, ultimate tensile strength, and other properties of materials through various mechanisms, including dislocation, solid solution, and precipitation. Wang et al[16] used the slurry fusion sintering technique to fabricate an in-situ (Ti, Nb, Mo)$_5$Si$_3$ dual-phase composite coating on the surface of C103 alloy. The surface layer of this coating is composed of a high-silicon phase of (Nb, Mo)Si$_2$, demonstrating remarkable composite gradient structure and oxidation resistance. In addition, Cai et a[2] prepared a novel YSZ-modified Si-Mo coating on the surface of TZM alloy via the slurry fusion sintering method. The resultant coating had an outer layer of (Mo, Zr)Si$_2$ and an inner layer of (Ta, W)Si$_2$, exhibiting excellent oxidation resistance and structural integrity. Sun et al[9] crafted a dual MoSi$_2$-based/NbSi$_2$ coating on Nb alloy using HAPC and SPS methods. However, this two-step preparation process is characterized by complex techniques and long-period preparation duration. Zhang[10–11] and Fu[12–13] et al employed HDS method to deposit a silicide coating on pure molybdenum plates and other substrates. The coating had uniform composition and a smooth surface, but this method caused high energy consumption at elevated temperatures, potentially impacting the mechanical properties of the substrate, which is unsuitable for precision parts. Consequently, the slurry fusion sintering method is more appropriate for coating preparation, and it is adopted in this research.

Silicide-based high-temperature protective coatings are the most widely applied ones for the tantalum alloys. In high-temperature oxidizing environments, a protective SiO$_2$ glass film is usually formed by the selective oxidation reaction of silicon. This glass film demonstrates unique viscous flow characteristics under high-temperature conditions, which can repair microcracks, pores, and other defects within the coating, exhibiting a certain degree of self-healing capability. Therefore, silicide coatings exhibit excellent oxidation resistance within the high-temperature range of 1000–1700 °C[2,4–8]. However, when the temperature surpasses the melting point of SiO$_2$ (1710 °C), the viscosity of the protective SiO$_2$ glass film drops sharply, diminishing the barrier effect against oxygen diffusion and significantly reducing the lifespan of coating[17–18]. When the ambient temperature rises to 1800 °C, the vapor pressure of SiO at the interface between the silicide and the SiO$_2$ glass film exceeds 100 kPa, resulting in active oxidation of the coating and subsequently degrading the protective performance[19]. Meanwhile, a significant mismatch exists in the coefficient of thermal expansion (CTE) of the high-silicon phase ceramic TaSi$_2$ (8.8×10^{-6} °C^{-1})[5], the oxidized SiO$_2$ glass film (0.55×10^{-6} °C^{-1})[20], and the tantalum alloy substrate (6.5×10^{-6} °C^{-1})[4]. Coupled with the inherent brittleness of TaSi$_2$ and SiO$_2$, the silicide coating on the tantalum alloy surface is prone to the formation of penetrating cracks or spalling during thermal cycling, ultimately leading to a significant reduction in the service life of coating.

The Hf-Ta-based ultra-high-temperature ceramic system[21–30] exhibits unique advantages in the field of extreme environment protection. Kiryukhantsev-Korneev et al[31–32] fabricated Mo-Si-B, Mo-Hf-Si-B, and other related coatings through combustion synthesis and hot pressing techniques. These coatings are compatible with a wide range of substrates. The incorporation of hafnium alleviates the brittleness of Mo-Si-B coatings and enhances their tribological properties. Furthermore, Mo-Hf-Si-B coatings demonstrate exceptional oxidation resistance. The doping of hafnium facilitates defect repair, which is attributed to the formation of a protective oxide layer composed of SiO$_2$ and HfO$_2$/SiO$_2$ on the coating surface. Notably, the Mo-Hf-Si-B coating deposited via direct current electrodeposition exhibits the shallowest oxide layer depth (approximately 4 μm) after oxidation tests. Most reports about Hf-Ta-Si focus on their application in C/C composites[33–36]. Tong et al[33] introduced tantalum into the matrix using the polymer infiltration-pyrolysis method to bolster the cyclic ablation performance of C/Hf-Si-C composites. The introduction of tantalum provides robust oxygen barrier and impact resistance properties for the ablated composites. Additionally, the stress degradation trend of the material shifts from a continuous decline to a stepwise one. The fiber pull-out length at the fracture site is markedly reduced, whereas the adhesion and compactness of the oxide film are significantly enhanced. As the core components of this system, TaC (melting point of 3880 °C) and HfC (melting point of 3950 °C) complement each other in performance, offering mechanical stability at 3000 °C and the highest melting point among binary ceramics, respectively. Notably, HfC not only exhibits ultra-high-temperature resistance but also generates HfO$_2$ (melting point of approximately 2800 °C) as the oxidation product. This product has a low saturated vapor pressure and a high CTE of 9.3×10^{-6} °C^{-1}[37], effectively forming a stable oxide layer[23–24]. This synergistic effect is further amplified in the Hf-Ta coating. The high-temperature oxidation process produces a special multiphase oxide Hf$_6$Ta$_2$O$_{17}$ for the protection of tantalum alloys. This oxide not only maintains the single-phase stability of the α-PbO$_2$-type orthorhombic structure (no phase transition occurs from room temperature to its melting point) but also possesses a high

melting point (approximately 2400 °C), low thermal conductivity, and appropriate thermal expansion characteristics which match well with those of the substrate (CTE=9.59×10^{-6} °C^{-1}), making it an ideal thermal structural protective layer[38–40]. These excellent thermal properties allow the Hf-Ta coating to serve stably at 1800 °C for long periods, and even provide effective short-term protection under extreme conditions at 2000 °C[41].

However, traditional Hf-Ta coatings face restrictions in oxygen-enriched atmospheric environments due to the high oxygen diffusion rate in their oxide films, resulting in inadequate oxygen barrier capabilities for the substrate. To overcome this bottleneck, this study introduced Si as a modifying element to construct a $HfO_2/Hf_6Ta_2O_{17}$-SiO_2 composite structure within the oxide film. This multiphase composite structure laid the foundation for subsequent oxidation regulation. During high-temperature oxidation, $Hf_6Ta_2O_{17}$ and HfO_2 jointly formed a rigid framework, stabilizing the SiO_2 glass phase through a pinning effect. Simultaneously, the flowing SiO_2 effectively fills the framework pores, forming a dense composite oxide film. This structural innovation endows the coating with threefold advantages: (1) the $HfO_2/Hf_6Ta_2O_{17}$ framework provides high-temperature strength and thermal expansion matching; (2) the SiO_2 glass phase inhibits oxygen diffusion and repairs microcracks; (3) the multiphase synergistic effect significantly enhances oxidation resistance, thermal shock resistance, and high-temperature erosion resistance. Through the coordinated regulation of composition design and diffusion kinetics, the modified Hf-Ta-Si coating may ultimately construct a gradient protective system, which is suitable for extreme thermal-mechanical-chemical coupled environments. This structural innovation and its impact mechanism require further investigation.

Therefore, this study used Ta12W alloy as the substrate and designed two types of high-Si slurries. By controlling the high-temperature diffusion reaction between the slurries and the Ta12W alloy substrate during the high-temperature vacuum melting and sintering processes, an in-situ Hf-Ta-Si coating was formed on the substrate surface. Additionally, during the vacuum reaction sintering process, the samples were vertically suspended, leveraging the flow characteristics of Si element under high-temperature conditions to swiftly cover the microstructure of target coating. This approach facilitated high-throughput preparation of the coating and clarified the influence mechanism of Si addition on the phase composition and microstructure of the Hf-Ta coating.

2 Experiment

Ta12W alloy was used as the substrate material. The pretreatment steps for the substrate material were as follows. Firstly, the alloy plate was processed into a sheet-like sample with dimensions of 75 mm×10 mm×1.5 mm. Then, the sample surfaces were sequentially polished using 180# and 600# sandpaper to remove oxide scales and cutting marks, followed by edge and corner chamfering. Subsequently, the sample underwent sandblasting treatment to achieve a rough surface. The sand used for the sandblasting process was ZrO_2 with particle size of 40–60 μm, and the sandblasting pressure was maintained at 5 MPa. Finally, the samples were immersed in an ethyl acetate solution for ultrasonic cleaning for 30 min. To prevent the influence of the oxygen-absorbing layer on the sample surface during coating preparation, the samples were etched with a mixed acid solution of hydrofluoric acid and nitric acid before slurry spraying.

Hf and Si powders were used as raw materials for the coating preparation, and the coating was prepared on the surface of Ta12W alloy substrate through a slurry reaction sintering process. Firstly, raw powder materials containing Hf (99.9wt% purity, particle size of 1–10 μm) and Si (99.9wt% purity, particle size of 1–5 μm) with mass ratios of 30∶70 and 40∶60 were accurately weighed using an electronic balance. A dispersant was formulated by blending nitrocellulose lacquer and ethyl acetate in a specified ratio, and then it was mixed with the powder to produce a slurry. The slurries prepared with Hf∶Si ratio of 30∶70 and 40∶60 were denoted as 30Hf-70Si and 40Hf-60Si slurries, respectively. Subsequently, the slurry was poured into an agate ball mill (500 mL, with a fixed number of balls) and placed in a planetary ball mill (XGB4 model, manufactured by Nanjing Boyuntong Instrument Technology Co., Ltd). The mill was set to rotate at the speed of 340 r/min with a milling cycle of clockwise rotation for 0.8 h, followed by counterclockwise rotation of 0.8 h, and the gap time was 0.4 h. After a total milling procedure of 48 h, two distinct Hf-Si coating slurries with different composition were obtained. Employing a portable handheld air spray gun (Iwata LPH-80-104G, Japan), the slurries of equal volume were dispensed sequentially with the spraying distance of approximately 25 cm. The slurry was then evenly applied onto the surface of the Ta12W alloy sample using the spray gun, followed by drying at 80 °C for 15 min. Finally, the sample was positioned inside a vacuum sintering furnace with vacuum level of no more than 1×10^{-3} Pa. Initially, it was heated at a rate of 10 °C/min to reach 800 °C and maintained at designed temperature for 30 min. Subsequently, the heating rate increased to 15 °C/min to achieve 1420 °C and then held for 60 min. Ultimately, the sample cooled down naturally within the furnace, forming the as-prepared coating.

X-ray diffractometer (XRD, Rigaku SmartLab, with a high-probability rotating anode) was employed with Cu as the target material. XRD analysis was operated at a voltage of 40 kV and scan speed of 2°/min with a step size of 0.02°. The scanning range 2θ was set as 20°–80°. The composition as well as surface and cross-section morphologies of the coatings were characterized by a field emission scanning electron microscope (SEM, SU-5000, Oxford, UK) coupled with an energy dispersive X-ray spectroscope (EDS, X-Max, Oxford, UK). The microstructure of the coating was further examined using a transmission electron microscope (TEM, Talos F200X, USA), and the phase composition of the micro-area was analyzed through selected area electron diffraction

(SAED). TEM samples were processed using focused ion beam (SEM FEI, VERSA 3D, America) technique.

Thermodynamic calculations were performed on the potential phases that may form during the growth process of the coating by commercial software packages HSC Chemistry v. 6.0 (Outokumpu Research Oy, Pori, Finland) and Facstage Education (Montreal, Canada and Aachen, Germany) to determine their phase stability.

3 Results

3.1 Microstructure and phase composition of 30Hf-70Si-Ta coating

Fig. 1 illustrates the appearances and XRD patterns of different areas of the as-prepared 30Hf-70Si-Ta coating on Ta12W alloys using 30Hf-70Si slurry, which is referred to as 30HS sample, after vacuum reaction sintering. Significant differences in surface morphology can be observed: four distinct characteristic areas can be distinguished from top to bottom of the sample. The surface at area 1 is flat and exhibits a silvery-white metallic luster; the surface morphology of area 2 is similar to that at area 1, but it has a slight striped pattern; the surface of area 3 is a mixed-color area of radial silvery-white and dark gray phases; the surface of area 4 is flat and dark gray. Fig. 1 also presents XRD patterns of different regions of the 30HS sample. The area 1–3 of the as-prepared coating mainly contain three phases: HfSi (PDF: 65-5750), HfC (PDF: 65-8750), and Hf_5Si_4 (PDF: 42-1166). The diffraction peak intensities of HfSi and Hf_5Si_4 increase near the bottom area of the sample, indicating higher concentrations of these phases in the bottom area. In contrast, the surface phase of area 4 is dominated by HfC. A minor amount of TaC (PDF: 19-1294) still exists on the surface, and two forms of carbon (PDF: 50-1082 and PDF: 26-1077) can also be detected.

Further characterization was conducted on the microstructures at various positions of the as-prepared 30HS sample.

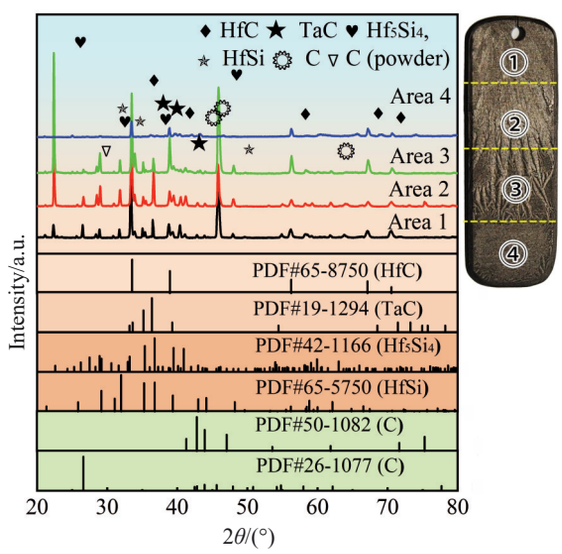

Fig.1 Appearances and XRD patterns of different areas of 30HS sample

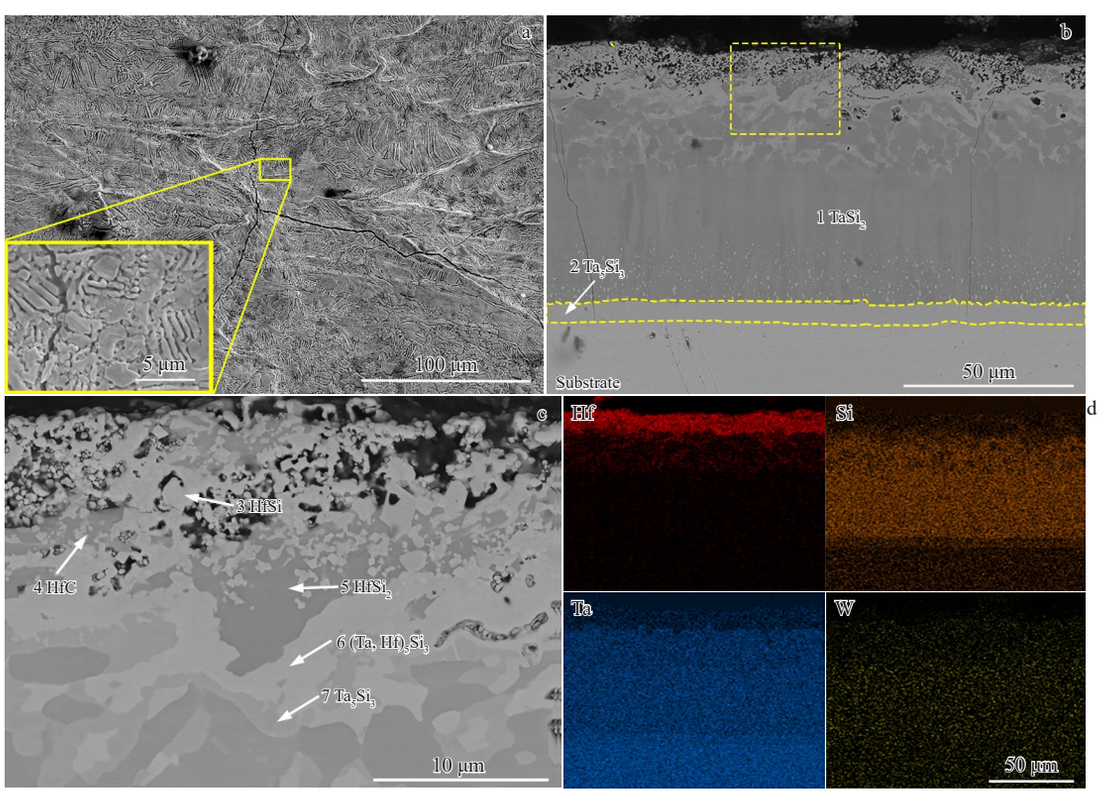

Fig.2 Surface morphology (a) and cross-section morphology (b) of area 1 of 30HS sample; magnified image of dotted rectangular area in Fig.2b (c); EDS mapping results corresponding to Fig.2b (d)

Fig. 2a–2b illustrate the surface and cross-section microstructures of area 1 of 30HS sample, respectively. As depicted in Fig. 2a, the coating surface of area 1 displays no discernible defects, such as pores, but contains a small number of cracks. According to Fig. 2c, it can be observed that the coating surface exhibits both flaky and striped morphologies. As shown in Fig.2b and 2d, it is evident that the coating thickness of area 1 is approximately 81 μm. The cross-section morphology exhibits a four-layer morphology: an upper layer of Hf-rich ceramic-metal composite, a middle layer of silicide, a lower layer of high-silicide, and a coating/substrate interface reaction layer. Moreover, the coating is entirely continuous and dense with only minor pores on the surface layer of the coating, as shown in Fig. 2c. Table 1 presents EDS analysis results of different locations depicted in Fig. 2. Based on the atomic ratio of elements, XRD results, and the Ta-Si[42] and Hf-Si[43] phase diagrams, it is preliminary determined that the main layer of the coating is identified as dark gray high-silicide phase $TaSi_2$ (point 1), whereas the interface reaction layer between the coating and the substrate is Ta_5Si_3 (point 2), and this layer thickness is approximately 6 μm. Combining EDS and XRD results, the light gray phase in the upper layer of the metal ceramic is identified as HfSi (point 3), the white contrast phase is HfC (point 4), and the dark gray phase is $HfSi_2$ (point 5). The middle layer is primarily composed of the Ta_5Si_3 medium-silicide phase with a substantial amount of Hf solid-solubilized in Ta_5Si_3 near the upper layer of the coating (point 6), whereas the Hf content significantly decreases in Ta_5Si_3 at the lower position (point 7).

Fig. 3a–3b show the surface and cross-section morphologies of area 2 of the as-prepared 30HS sample, respectively. As shown in Fig. 3a, the coating surface is smooth with minor cracks and localized granular particles, but no obvious defects, such as pores, can be observed. The local magnification

Table 1 Composition of different points marked in Fig.2 (at%)

Point	C	Si	Hf	Ta	W
1	-	70.3	0.9	28.3	0.5
2	-	43.0	2.0	52.9	2.1
3	-	58.8	34.9	6.3	-
4	64.7	-	27.8	7.2	0.3
5	-	67.6	25.5	6.7	0.2
6	-	47.1	23.7	26.4	2.8
7	-	57.2	9.4	29.1	4.3

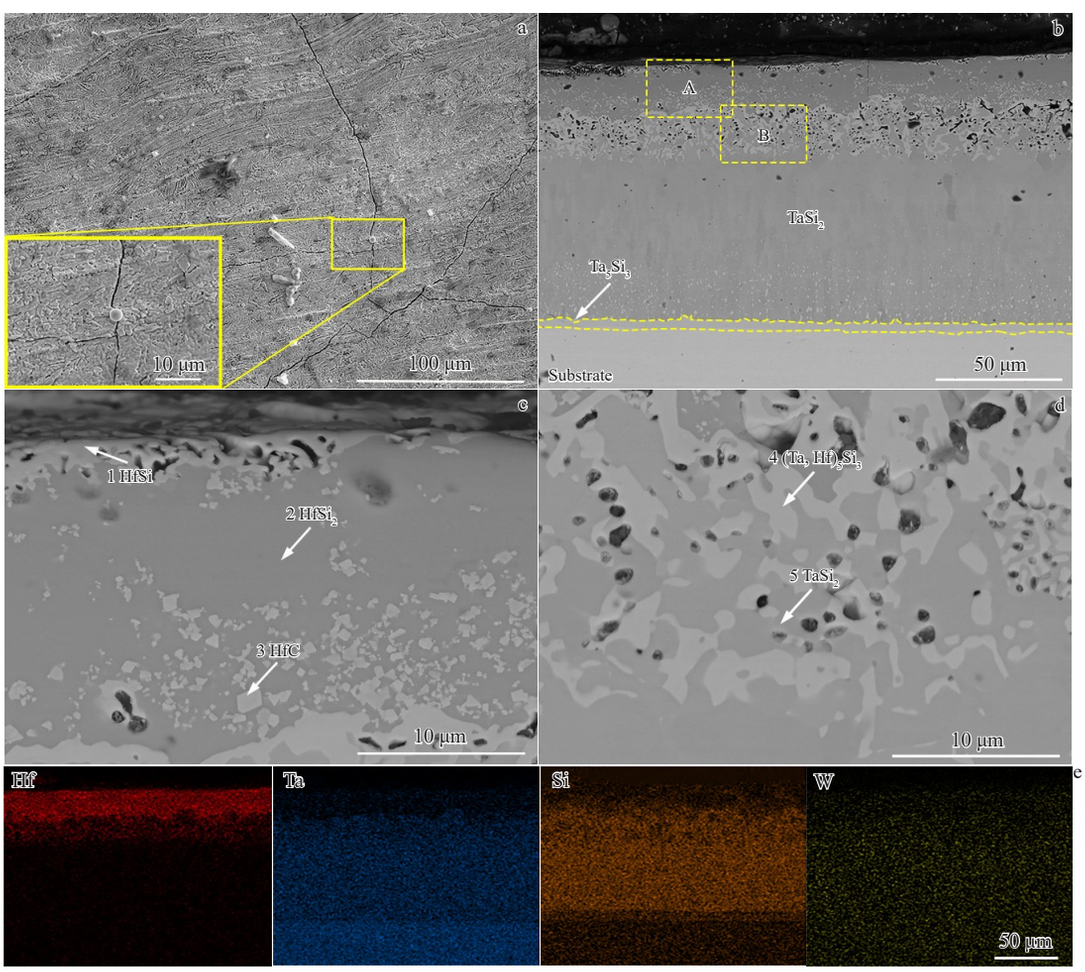

Fig.3 Surface morphology (a) and cross-section morphology (b) of area 2 of 30HS sample; magnified images of dotted rectangular area A (c) and area B (d) in Fig.3b; EDS mapping results corresponding to Fig.3b (e)

reveals that some granular particles are pinned within the cracks on the coating surface. Fig. 3b shows that the coating thickness is approximately 107 μm, exhibiting a distinct layered dense structure. Table 2 shows the composition of different points marked in Fig. 3. It can be seen that the lower high-silicide layer and the coating/substrate interface reaction layer of area 2 have the same phases as those of area 1, predominantly consisting of $TaSi_2$ and Ta_5Si_3, but the thickness of interface reaction layer is about 4 μm. However, the upper metal-ceramic layer (Fig. 3c) exhibits a more uniform structure, containing a higher proportion of $HfSi_2$ and a smaller amount of HfC and HfSi. Additionally, the middle silicide layer still contains a significant amount of $(Ta, Hf)_5Si_3$.

Table 2 Composition of different points marked in Fig.3 (at%)

Point	C	Si	Hf	Ta	W
1	-	47.4	43.7	8.1	0.8
2	-	67.8	26.2	6.0	-
3	63.0	-	32.9	4.1	-
4	-	48.1	26.5	22.5	2.9
5	-	70.6	3.3	23.4	2.7

Fig. 4a – 4b depict the surface and cross-section morphologies of area 3 of the 30HS sample, respectively. As shown in Fig. 4a, the coating surface displays a wavy morphology with a few cracks, but no significant defects, such as pores, can be observed. Furthermore, the darker contrast areas correspond to Si-rich regions. Fig.4b–4d show the cross-section morphologies of the 30HS sample. It can be seen that the thickness is approximately 118 μm. A three-layer structure can be observed: an upper ceramic-metal composite layer, a middle high-silicide matrix layer, and a coating/substrate interface reaction layer. Table 3 shows the composition of different points marked in Fig. 4. According to Table 3, the upper layer of the coating is enriched with Hf, HfC particles are dispersed within $HfSi_2$, and a significant amount of Si is also enriched in this layer. Additionally, a transition zone (point 5) exists between the Si-rich region and the main layer, where a small amount of element Hf is dissolved. The main layer of the coating mainly consists of $TaSi_2$, and dispersed Ta_5Si_3 particles exist beneath the main layer. Due to the high Si content in the coating, the intermediate ceramic layer and the medium-silicide Ta_5Si_3 in the interface reaction layer are transformed into $TaSi_2$. This result leads to the disappearance of the medium-silicide layer, and the thickness of the interface

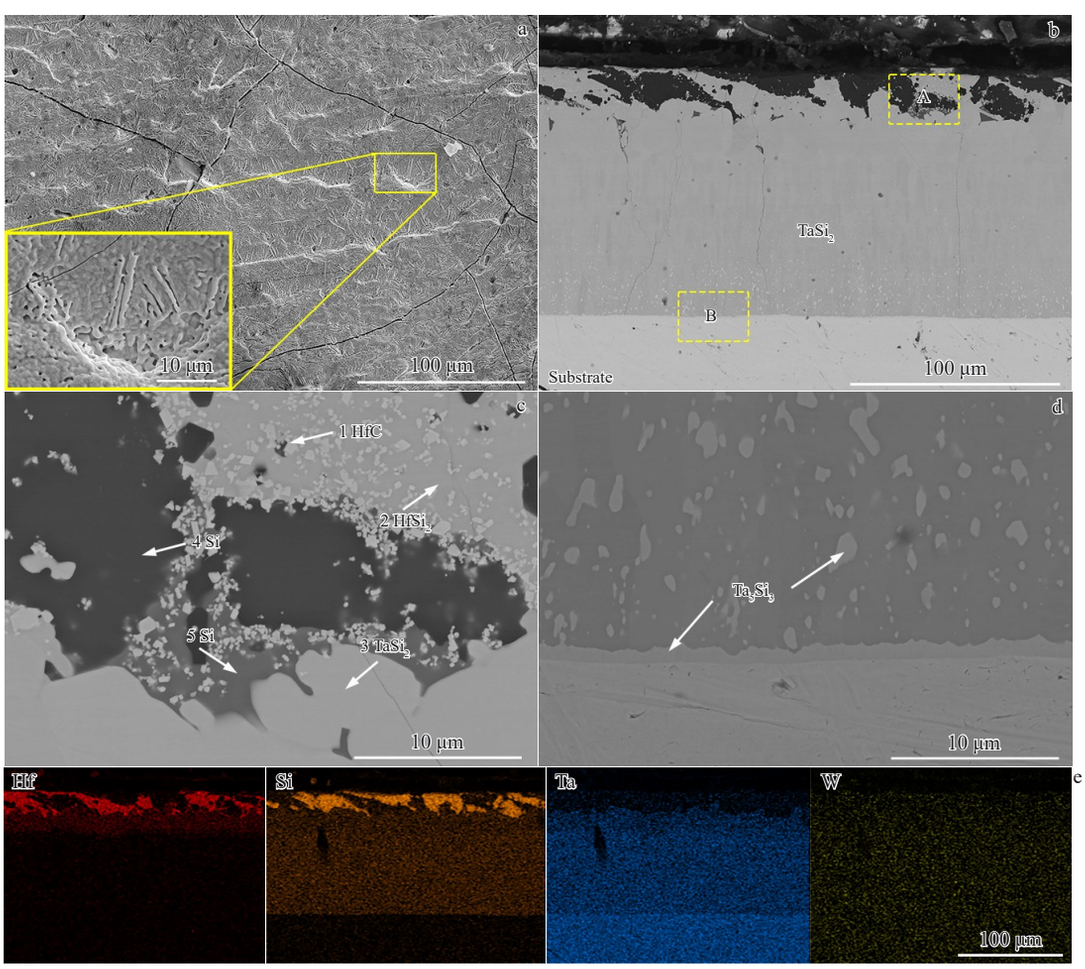

Fig.4 Surface morphology (a) and cross-section morphology (b) of area 3 of 30HS sample; magnified images of dotted rectangular area A (c) and area B (d) in Fig.4b; EDS mapping results corresponding to Fig.4b (e)

reaction layer between the coating and the substrate is significantly thinner than that of area 1 and area 2. The thickness of the interface reaction layer of area 3 is only 1 μm and this layer is light gray.

Table 3 Composition of different points marked in Fig.4 (at%)

Point	C	Si	Hf	Ta	W
1	66.4	0.4	30.6	-	2.6
2	-	63.9	32.5	3.6	-
3	-	68.9	9.0	20.5	1.6
4	-	99.9	0.1	-	-
5	-	82.5	13.3	3.6	0.6

Fig. 5a – 5b present the surface and cross-section morphologies of area 4 of the 30HS sample, respectively. As shown in Fig. 5a, the coating surface is porous and granular without obvious microcracks. According to Fig. 5b – 5d and EDS mapping results (Table 4), it can be seen that the overall thickness of the coating is approximately 250 μm. The cross-section morphology can still be divided into three layers: an upper thick ceramic-metal composite layer, a middle high-silicide layer, and a lower extremely thin interface reaction layer (thickness of approximately 0.7 μm). The upper layer of the coating mainly contains striped $HfSi_2$ and a large amount of undissolved Si. The main layer consists of $TaSi_2$. In the transition zone, a trace amount of Ta and W is dissolved in Si. Due to the primary enrichment of Si on the surface, the coating/substrate interface reaction layer is relatively thin.

The morphology differences of different areas of 30HS sample are primarily attributed to the gravitational flow of a large amount of molten Si from top to bottom. This flow results in relatively smooth appearance of area 1 – 2 with striped and channel-like microstructures. Area 3 exhibits a striped and channel-like morphology at the macroscale, and its microstructure displays wavy undulations. Area 4 is flat, but its microstructure contains a significant amount of unsintered and accumulated Si. Consequently, the slurry composition can be optimized by reducing the Si content.

3.2 Microstructure and phase composition of 40Hf-60Si-Ta coating

Fig.6 shows the appearances and XRD patterns of different areas of the as-prepared 40Hf-60Si-Ta coating using the 40Hf-60Si slurry after vacuum reactive sintering, which is referred to as 40HS sample. The coating surface exhibits three distinct morphological features. The top area (area 1) is flat and

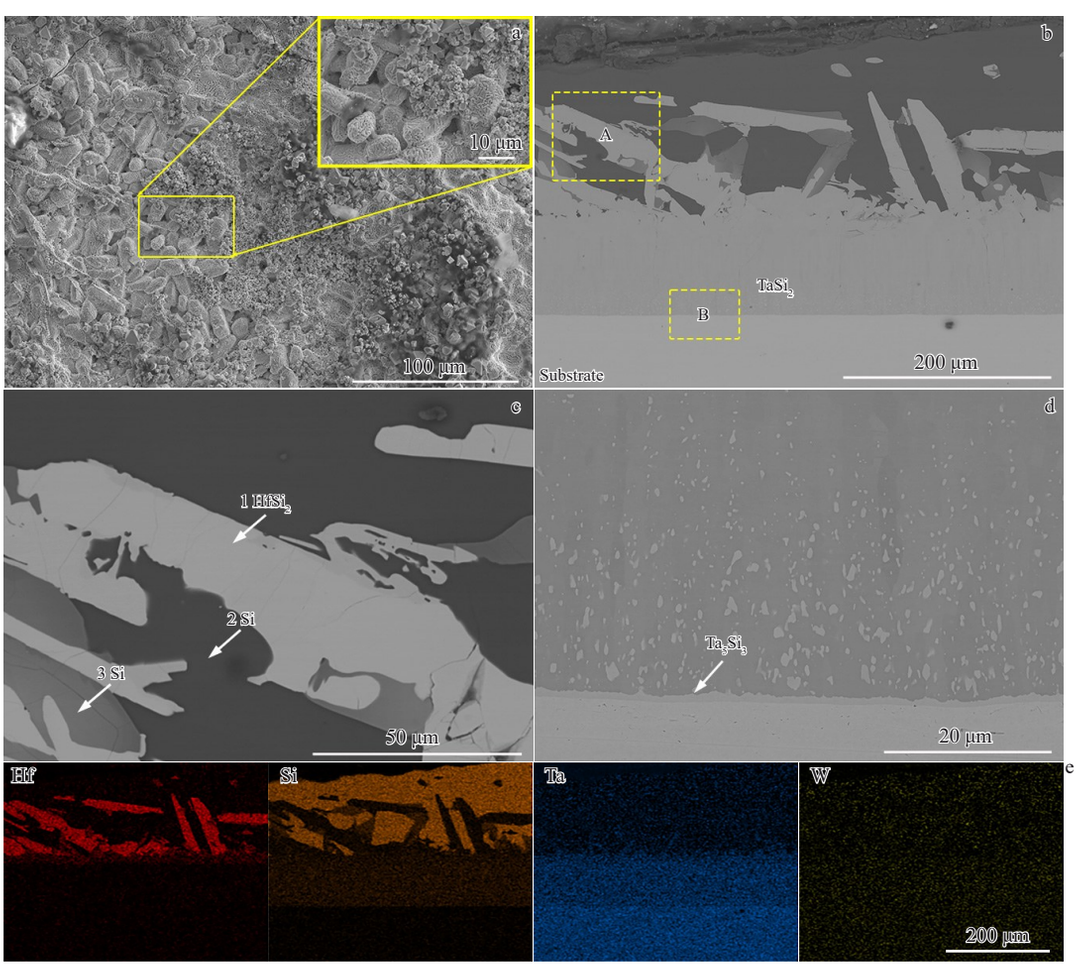

Fig.5 Surface morphology (a) and cross-section morphology (b) of area 4 of 30HS sample; magnified images of dotted rectangular area A (c) and area B (d) in Fig.5b; EDS mapping results corresponding to Fig.5b (e)

predominantly dark gray. The middle area (area 2) displays a slightly striped surface morphology. The bottom area (area 3) is relatively smooth and exhibits a shiny appearance. XRD

Table 4 Composition of different points marked in Fig.5 (at%)

Point	Si	Hf	Ta	W
1	64.1	32.3	3.6	-
2	99.9	0.1	-	-
3	93.5	0.5	2.1	3.9

patterns reveal that the area 1 – 2 primarily consist of HfSi (PDF: 65-5750), HfC (PDF: 65-8750), and Hf_5Si_4 (PDF: 42-1166). Notably, XRD pattern of area 3 exhibits a distinct diffraction peak of element Si, indicating the presence of undissolved Si on the coating surface.

Fig. 7a – 7b illustrate the surface and cross-section morphologies of area 1 of 40HS sample, respectively. As shown in Fig. 7a, the coating surface displays a small number of cracks and micropores, and the surface is plate-like and planar. According to Fig. 7b – 7d, the coating thickness is approximately 89 μm, and the coating is continuous and dense

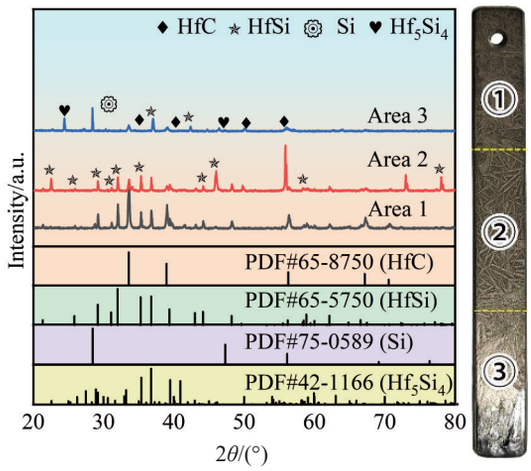

Fig.6 Appearances and XRD patterns of different areas of 40HS sample

with a four-layer structure: an upper Hf-rich ceramic-metal composite layer, a middle medium-silicide layer, a lower high-silicide layer, and a coating/substrate interface reaction layer. Table 5 lists the composition of different points marked in

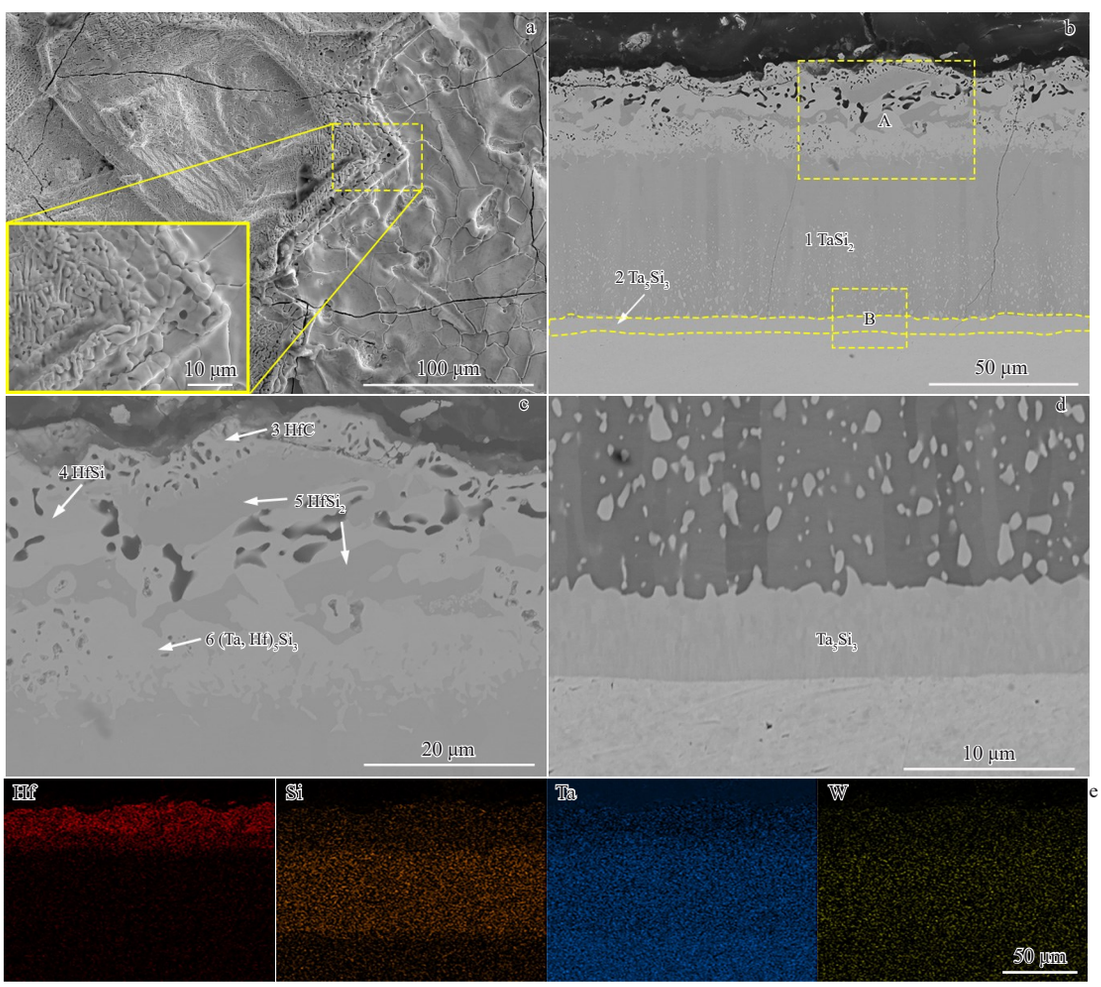

Fig.7 Surface morphology (a) and cross-section morphology (b) of area 1 of 40HS sample; magnified images of dotted rectangular area A (c) and area B (d) in Fig.7b; EDS mapping results corresponding to Fig.7b (e)

Fig. 7. Combining the XRD results and the Ta-Si[42] and Hf-Si[43] phase diagrams, the phases of each layer are as follows: the outermost surface of the upper metal-ceramic layer mainly contains HfC; the sub-surface layer contains HfSi and $HfSi_2$; the middle medium-silicide layer is mainly composed of continuous $(Ta, Hf)_5Si_3$; the lower high-silicide layer is predominantly $TaSi_2$. The interface reaction layer between the coating and the substrate consists of Ta_5Si_3 and its thickness is approximately 5 μm. These results are basically the same as those of the 30HS sample.

Fig. 8a–8b show the surface and cross-section morphologies of area 2 of 40HS sample, respectively. As shown in Fig. 8a, the plate-like morphology characteristic of the coating surface is no longer prominent. Instead, the surface exhibits a smoother planar morphology with minor cracks. As depicted in Fig. 8b, the thickness of area 2 of the as-prepared 40HS sample is approximately 121 μm, and the cross-section also has a four-layer structure. Table 6 lists the composition of different points marked in Fig. 8. According to EDS results in Table 6, the upper ceramic-metal composite layer primarily consists of HfSi, $HfSi_2$, and HfC. The middle medium-silicide layer contains $(Ta, Hf)_5Si_3$ dispersed within $TaSi_2$. The lower main layer is predominantly composed of $TaSi_2$ with a significant amount of Ta_5Si_3 dispersed at the bottom region. The interface reaction layer between the coating and the substrate is about 2.4 μm in thickness, and its phase is identical to that of area 1 of 40HS sample.

Table 5 Composition of different points marked in Fig.7 (at%)

Point	C	Si	Hf	Ta	W
1	-	70.6	1.6	25.8	2.0
2	-	43.7	1.3	49.2	5.8
3	65.9	-	30.2	3.9	-
4	-	46.8	48.7	4.3	0.2
5	-	65.3	29.5	5.0	0.2
6	-	46.4	24.1	26.9	2.6

Fig. 9a–9b show the surface and cross-section morphologies of area 3 of 40HS sample, respectively. As shown in Fig. 9a, the coating surface displays local peeling phenomenon, the upper surface exhibits a planar morphology, and the peeling areas show a lath-like morphology. Notably, no significant cracks are detected at this area. As depicted in Fig. 9b, the thickness of area 3 is approximately 198 μm, and its cross-section morphology consists of three layers: an upper ceramic-metal composite layer, a middle high-silicide layer, and a

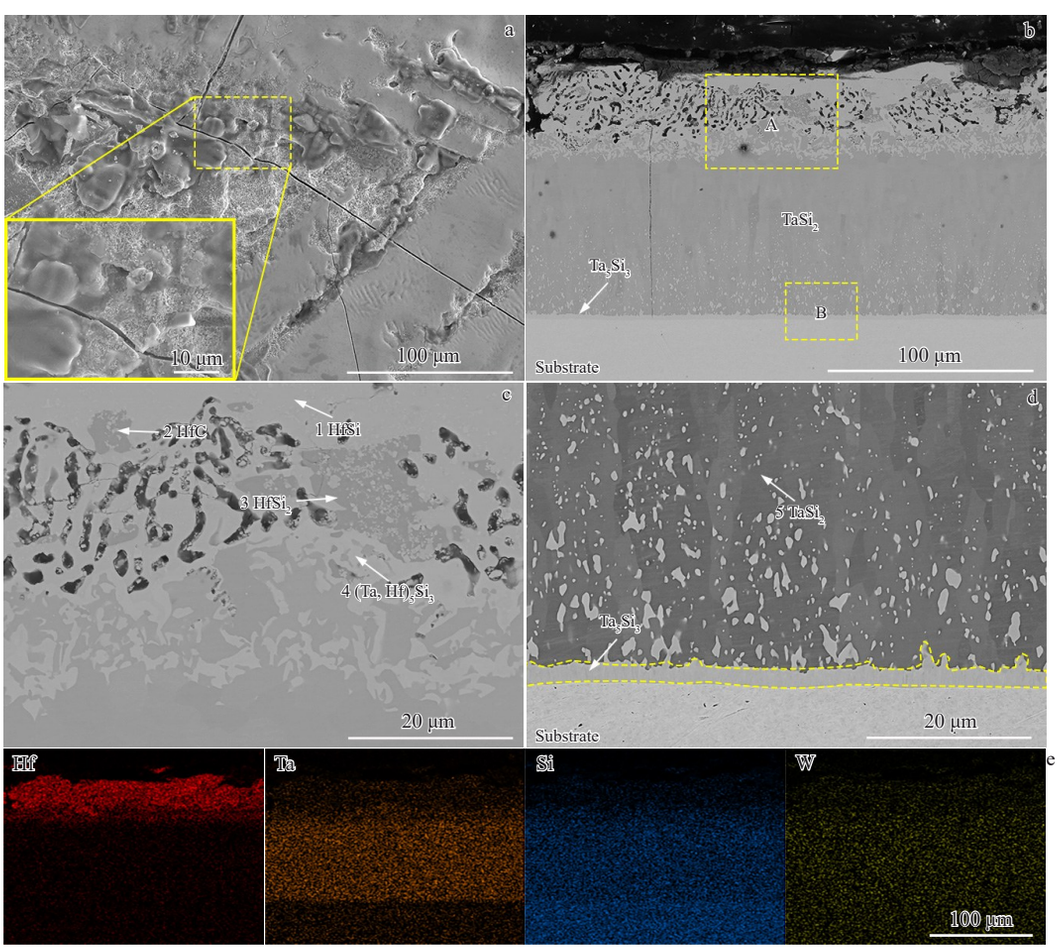

Fig.8 Surface morphology (a) and cross-section morphology (b) of area 2 of 40HS sample; magnified images of dotted rectangular area A (c) and area B (d) in Fig.8b; EDS mapping results corresponding to Fig.8b (e)

lower coating/substrate interface reaction layer. Table 7 lists the composition of different points marked in Fig. 9. According to EDS results in Table 7, the outer part of the ceramic-metal composite layer on the surface has a large amount of Si (point 4 in Fig.9c) and contains light gray phases of (Ta, Hf)Si_2 (point 2 in Fig.9c). At the interface between Si and (Ta, Hf)Si_2, some white HfC particles (point 1) are precipitated, whereas the dark gray phase at point 3 represents Si with a small amount of dissolved Ta and W. Furthermore, the main phase of area 3 and the phase of the interface reaction layer are $TaSi_2$ and Ta_5Si_3, respectively. The interface reaction layer is very thin of approximately 0.9 μm in thickness.

To further ascertain the precise phase composition of the upper ceramic-metal composite layer, TEM analysis was conducted on the area 2 of as-prepared 40HS sample. Fig. 10 presents the microstructures of the ceramic-metal composite layer and SAED patterns at different locations. Table 8 lists EDS analysis results of points marked in Fig. 10. Fig. 10a shows the high-angle annular dark field (HAADF) image of the area 2 of 40HS sample. It can be seen that HfC ceramic particles are embedded within the silicide ceramic matrix in the outermost layer of the coating, accompanied by a small number of pores. SAED pattern of area B in Fig.10a (Fig.10d) indicates that the white ceramic particles in the outermost layer are HfC. Fig.10c and 10g exhibit amorphous halo rings, corresponding to an amorphous structure. Thus, the specific phase cannot be determined. Based on EDS results in Table 8, region A is identified as the HfTaSi phase, which is brighter

Table 6 Composition of different points marked in Fig.8 (at%)

Point	C	Si	Hf	Ta	W
1	-	42.1	52.3	5.1	0.5
2	65.8	-	32.6	1.3	0.3
3	-	63.1	31.1	5.3	0.5
4	-	42.6	33.6	20.9	2.9
5	-	68.1	0.5	28.1	3.3

Table 7 Composition of different points marked in Fig.9 (at%)

Point	C	Si	Hf	Ta	W
1	63	-	32.9	4.1	-
2	-	66.7	15.1	16.3	1.9
3	-	89.1	0.4	4.6	5.9
4	-	100.00	-	-	-

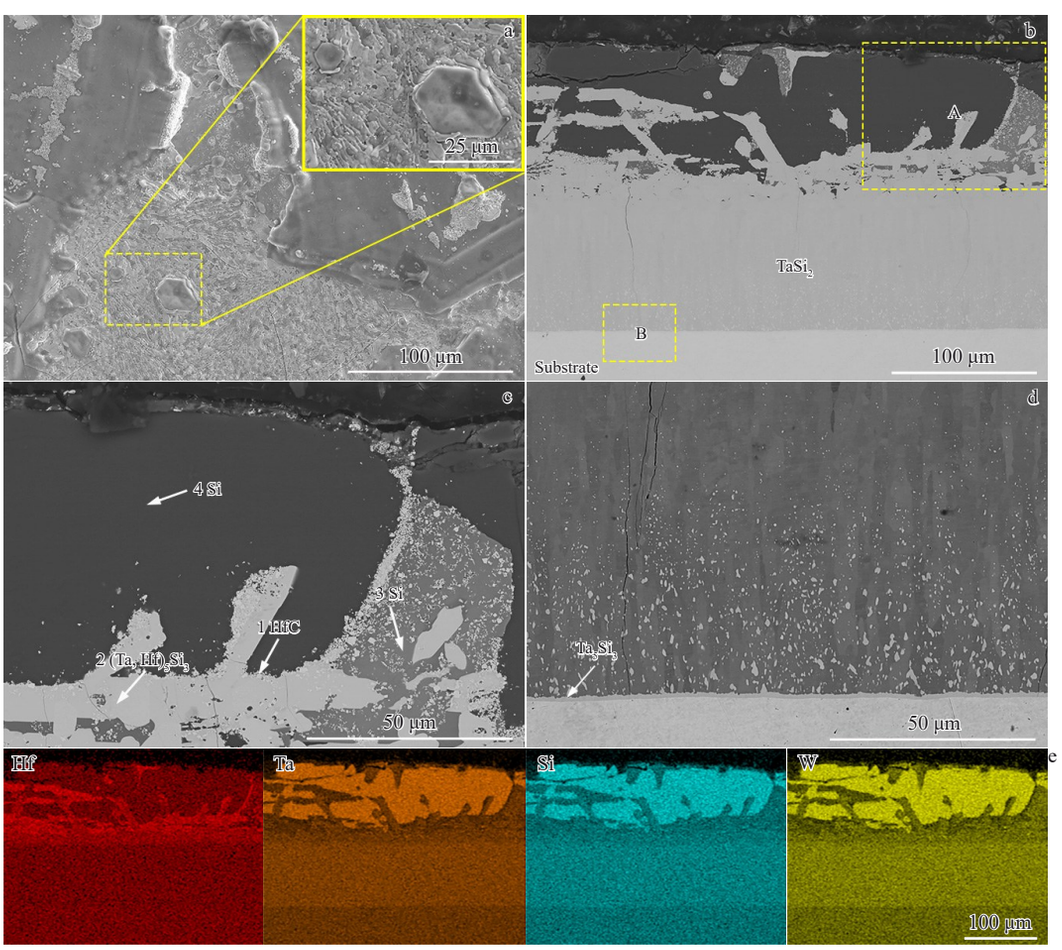

Fig.9 Surface morphology (a) and cross-section morphology (b) of area 3 of 40HS sample; magnified images of dotted rectangular area A (c) and area B (d) in Fig.9b; EDS mapping results corresponding to Fig.9b (e)

compared with the area C and D, suggesting that it is a medium-silicide phase. Meanwhile, area E is determined to be the HfTa phase, which is formed during the vacuum reaction sintering process when Ta atoms diffuse from the matrix and dissolve in the unreacted Hf powder.

SAED pattern of area D indicates the presence of HfTaSi ceramic phase, whereas the SAED pattern of area C reveals distinct amorphous rings, which further suggests the presence of HfTaSi particles in area D. EDS characterization reveals that area F–H are all composed of HfC ceramic phase. High-resolution characterization of area I is shown in Fig. 10h. The lower-left area exhibits distinct lattice fringes characteristic of the HfC ceramic phase, whereas the upper-right area shows no such fringes, indicating the presence of the HfTaSi phase. Fig. 10i is a local magnified image of Fig. 10h, and the calculated interplanar spacing is approximately 0.263 nm.

Based on the comprehensive TEM results, the medium-siliconized hafnium region on the coating surface is amorphous, making it impossible to definitively identify the specific phase as HfSi or Hf_5Si_4. Through TEM analysis, $HfSi_2$ can be confirmed as the HfTaSi ceramic phase, and some regions are amorphous.

Comparing 30HS and 40HS samples, it is observed that both coatings exhibit non-uniform surface morphologies in their as-prepared states. The surface of 30HS sample can be differentiated into four characteristic morphologies, whereas the surface uniformity of the 40HS sample shows great improvement: its surface features three typical zones. It is found that the structures of the two coatings are similar, featuring an Hf-rich ceramic-metal composite layer composed of HfC ultra-high-temperature ceramics, HfSi, and $HfSi_2$ on the surface, and a middle layer of Ta_5Si_3 with a substantial amount of Hf dissolved in solid solution. Both coatings have the main layer phase of $TaSi_2$ and interface reaction layer phase of Ta_5Si_3, and the thickness of the interface reaction layer is 5–6 μm. The cross-section morphologies of area 2 of both 30HS and 40HS samples exhibit similarities: they both contain a surface layer, an intermediate layer, a main layer, and an interface reaction layer. Notably, excessive micropores exist within the intermediate layer. The phase composition and uniformity of these four structures remain consistent and align well with each other. However, a notable difference arises: the outermost layers of 30HS sample contain a substantial amount of $HfSi_2$, whereas those of 40HS sample contain HfSi. This variation stems from the reduced Si content. The area 3 of both 30HS and 40HS samples shows the enrichment of Si in the samples. The evident segregation of Si is strongly correlated with the gravitational pull exerted by liquid silicon during the vacuum melting process. Despite these variations, the overall structures of the three coatings share similarities. Notably, the Si enrichment in the area 3 of 30HS sample is relatively less pronounced, compared with that at the other two areas. Due to the accumulation of Si, the surface phase is composed of HfC ceramic and $HfSi_2$. The excessive Si catalyzes the rapid reaction of the intermediate layer phase Ta_5Si_3 into the main layer phase $TaSi_2$. Consequently, the cross-sections of these three areas do not exhibit an intermediate layer, and the interface reaction layer is exceedingly thin of approximately 1 μm in thickness.

High-throughput coating preparation can be achieved by vertically suspending samples, ultimately yielding the targeted microstructure within the area 1 of the 40HS sample. This area features a pronounced gradient distribution in its microstructure, indicating an in-situ formed composite coating. The surface layer of the coating contains ultra-high temperature ceramics, namely HfC and Hf-Si ceramics, showing a low porosity. The middle layer is predominantly composed of a continuous $(Ta, Hf)_5Si_3$ silicide, whereas the lower layer is mainly characterized by high-silicide component $TaSi_2$. The interface reaction layer between the coating and the substrate consists of Ta_5Si_3. This gradient structure can effectively alleviate the thermal mismatch between the substrate and the coating, preventing interfacial delamination under rapid cooling and heating. Additionally, the elastic modulus of each layer gradually changes, reducing stress concentration caused by external impact or cyclic loading, and enhancing the resistance against spalling.

4 Discussion

4.1 In-situ reaction mechanism of Hf-Ta-Si coating

In this study, pure Si and Hf powders were used as the raw materials to prepare Hf-Ta-Si layered composite coatings on Ta12W substrates via slurry vacuum melting and sintering processes. During the vacuum melting and sintering process, Si in the slurry, which is located in the upper layer and has a lower melting point, preferentially melts to form a liquid Si phase. In this process, the metallic Hf powder is encapsulated by the molten Si, which also wets the Ta12W substrate. Subsequently, through thermal diffusion, the molten Si reacts with the metal powder and the substrate to form various silicide ceramic phases.

The two Hf-Ta-Si coatings exhibit significant morphology differences from top to bottom region, which are attributed to the varying Si content on the Ta12W alloy surface during the high-temperature vacuum reaction sintering process. At the initial stage of sintering, Si in the slurry melts, the liquid Si wets the Ta12W substrate, and the metal powder particles within the slurry are pre-layered. However, due to the vertical suspension of the samples and the strong fluidity of the molten Si on the sample surface, the molten Si flows towards the lower end of the sample under gravity, leading to notable variations in the Si content across different regions of the coating. As illustrated in Fig. 5 and Fig. 9, the surface layer of the coating at the bottom region contains a significant amount of unreacted Si. Two types of Hf-Ta-Si coatings display a layered morphology from the outer to the inner regions at various locations. The formation of the layered composite coating is directly associated with the thermodynamic and kinetic processes under specific conditions during the vacuum sintering of the slurry. During the high-temperature sintering process, 11 chemical reactions may occur, as follows:

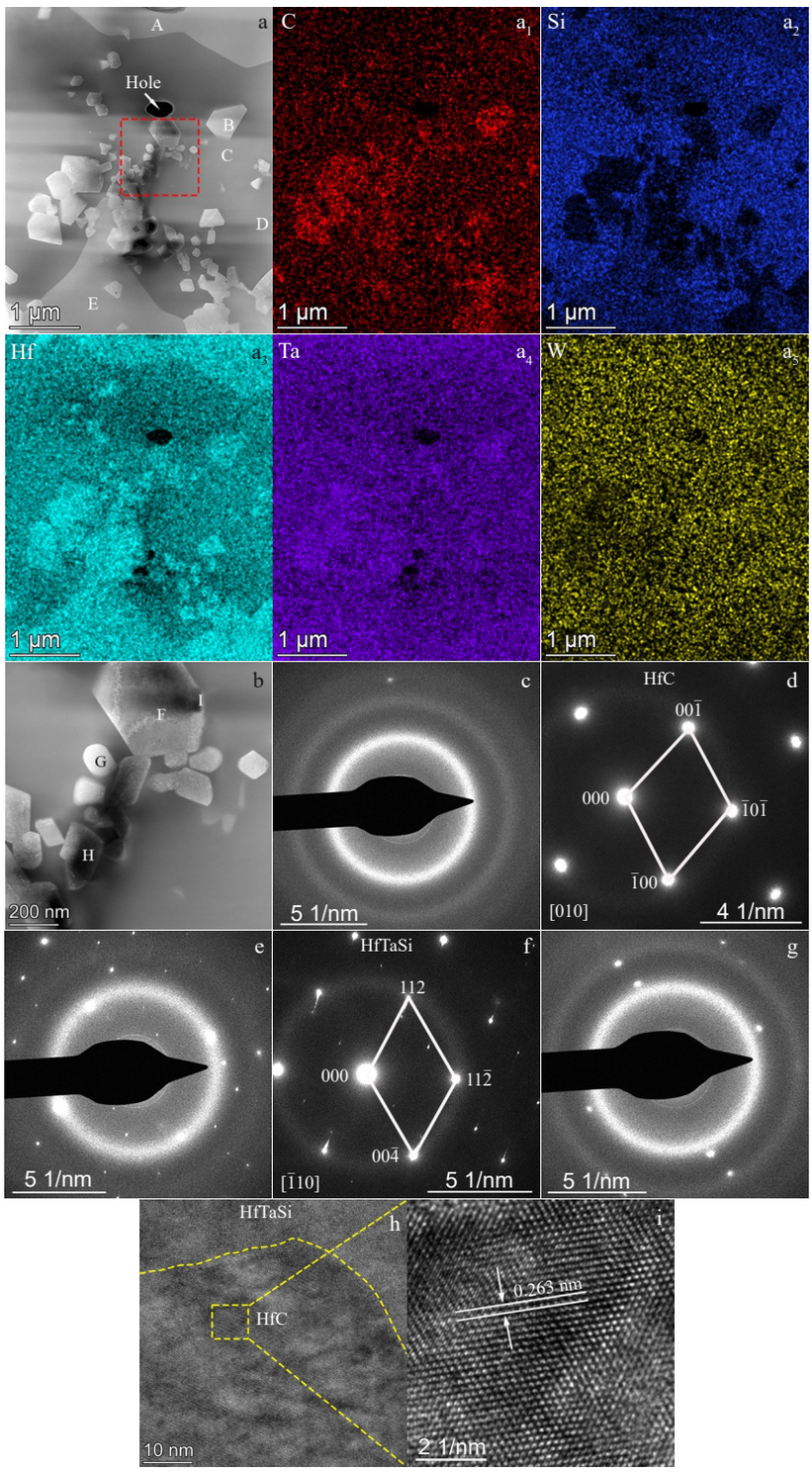

Fig.10 HAADF image (a) and corresponding EDS elemental mapping results (a_1–a_5) of area 2 of 40HS sample; magnified image of red-dotted rectangular area in Fig.10a (b); SAED patterns of area A (c), area B (d), area C (e), area D (f), and area E (g) marked in Fig.10a; high-resolution TEM image (h) and local magnified image (i) of area I in Fig.10b

$$Hf + Si = HfSi \quad (1)$$

$$5/4Hf + Si = 1/4Hf_5Si_4 \quad (2)$$

$$1/2Hf + Si = 1/2HfSi_2 \quad (3)$$

$$HfSi + Si = HfSi_2 \quad (4)$$

$$1/6Hf_5Si_4 + Si = 5/6HfSi_2 \quad (5)$$

$$Hf + Ta + Si = HfTaSi \quad (6)$$

$$1/2Ta + Si = 1/2TaSi_2 \quad (7)$$

$$5/3Ta + Si = 1/3Ta_5Si_3 \quad (8)$$

$$1/7Ta_5Si_3 + Si = 5/7TaSi_2 \quad (9)$$

$$1/2W + Si = 1/2WSi_2 \quad (10)$$

Table 8 Composition of different areas marked in Fig.10 (at%)

Area	C	Si	Hf	Ta	W
A	3.4	25.7	42.7	28.2	-
B	21.4	-	44.2	34.4	-
C	7.9	29.8	34.7	27.6	-
E	2.0	-	55.2	42.8	-
F	24.5	-	46.5	29.0	-
G	27.1	-	42.4	30.5	-
H	20.6	-	43.2	36.2	-

$$5/3W + Si = 1/3W_5Si_3 \quad (11)$$

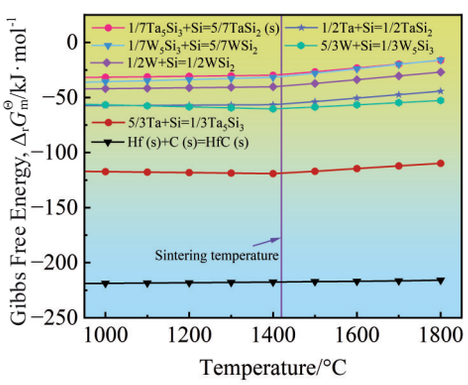

Fig.11 $\Delta_rG_m^\Theta$-T curves of possible reactions during coating preparation process

Fig.11 illustrates the Gibbs free energy ($\Delta_rG_m^\Theta$) variation as a function of temperature (T) for different reactions involved in the formation of the Hf-Ta-Si layered composite coatings. It reveals that the $\Delta_rG_m^\Theta$ values for all reactions are less than 0, indicating that the reactions can spontaneously proceed within the corresponding temperature ranges. During the initial stage of sintering, due to the lower melting point of Si, Si melts firstly to form a liquid Si phase. The liquid Si covers the Hf powder and reacts with Hf to produce the corresponding silicides[44]. At this stage, the reactions primarily involve the formation of Ta silicides. Notably, the Gibbs free energy corresponding to Eq.(8) is more negative, suggesting that this reaction is thermodynamically more favorable and preferentially forms Ta_5Si_3. Concurrently, liquid Si wets the Ta12W substrate, and Hf and Si atoms undergo different degrees of interdiffusion with the substrate. Since the diffusion coefficient of molten Si is much higher than that of solid metal Hf, Si rapidly reacts with the substrate to form a Ta_5Si_3 transition zone. Subsequently, the growth of the interface reaction layer is primarily controlled by the diffusion process of Si. As the interdiffusion of Si and Ta continues, excessive Si gradually reacts with Ta, and Ta_5Si_3 is transformed into $TaSi_2$, according to Eq. (7 – 9), which accumulates continuously to form the main layer of the coating. When the Si content in a certain region becomes insufficient, an intermediate layer of Ta_5Si_3 forms above the main layer. This reaction process and mechanism are closely related to the coating structure and composition changes.

Fig.12 depicts the formation mechanism of microstructures of different regions of coating on Ta12W alloy surface during vacuum reactive sintering process. A notable phenomenon is observed: no middle layer is formed at the bottom regions. In conjunction with the aforementioned reaction mechanism, this is because during the vacuum sintering process, a significant amount of molten Si flows towards the bottom of the sample under gravity, leading to an enrichment of Si at the bottom. In

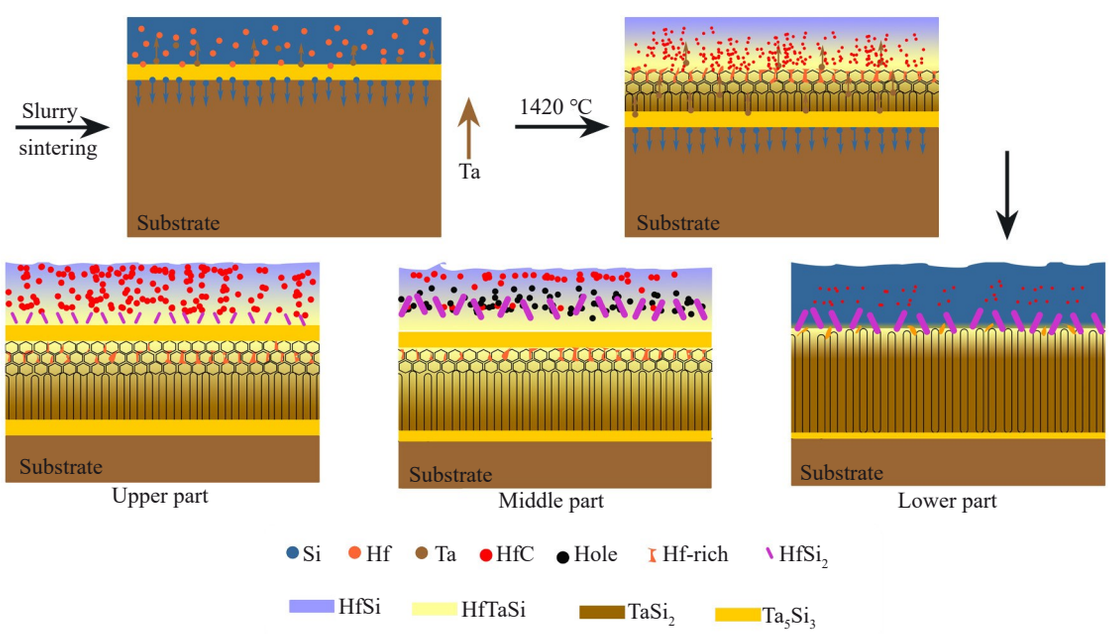

Fig.12 Schematic diagrams of formation mechanism of microstructures of different regions of coating on Ta12W alloy surface during vacuum reactive sintering process

this Si-rich region, Ta_5Si_3 is completely transformed into $TaSi_2$, eliminating the possibility of the formation of middle layer.

In the upper part of the sample, the reactions primarily involve Eq. (1 – 6), resulting in the formation of Hf-based ceramics and a minor amount of $HfSi_2$. In the middle part of the sample, although Eq.(1–6) are also involved, the relatively higher Si content leads to a significant increase in the amount of $HfSi_2$ in the products. At the bottom region of the sample, the Si content is much higher than that in the upper and middle parts, so an environment with excessive Si is formed. Thus, the coating surface primarily undergoes the reaction of Eq. (4), resulting in a large amount of $HfSi_2$ ceramic. Simultaneously, due to the short duration of the sintering reaction, Si cannot fully diffuse into the substrate for participation in the reaction, leading to unreacted Si on the surface and ultimately causing the non-uniform surface morphology. The differences in reactions and surface morphology at different parts are closely related to the coating composition design, preparation process, as well as reaction thermodynamics and kinetics. This result provides important research solutions for optimizing the performance of Hf-Ta-Si composite coatings.

4.2 Reaction mechanism of HfC ceramic in coating

During the coating preparation process, metallic Hf forms the HfTaSi phase through a solid solution reaction. The acid-alcohol resin contained in the organic solvent undergoes pyrolysis in an inert atmosphere to obtain glassy C[45], inducing the bulk precipitation of HfC. This resultant product is expected to enhance the oxidation resistance and high-temperature stability of coating. Since the diffusion coefficient of molten Si is much greater than that of solid metallic Hf, the remaining Hf experiences restricted diffusion due to its larger atomic size. This phenomenon leads to the enrichment of HfSi/Hf_5Si_4 phases in the surface layer during subsequent reactions[44] and the formation of an elemental gradient distribution at grain boundaries of Ta_5Si_3[46]. Notably, although the intrinsic diffusion rates of Ta and W are low, their migration ability is significantly enhanced by the solid-liquid diffusion mechanism in the molten Si, which results in the ubiquitous segregation of Ta in Hf-based silicides[47]. Area 2 of 30HS and 40HS samples shares a high degree of similarity. Although the surface layer of the coatings exhibits dense structure, a considerable number of micropores are observed beneath the surface. The primary phases present in these regions are Ta_5Si_3, HfC, and HfTaSi, and Ta_5Si_3 accounts for the largest volume fraction. These pores are primarily attributed to the volume contraction during the formation of Ta_5Si_3. Furthermore, HfC ultra-high-temperature ceramic particles with different sizes are dispersed around Ta_5Si_3, impeding the agglomeration and growth of Ta_5Si_3 during the vacuum sintering process. This is the underlying cause of the increased porosity at area 2 in both coatings. The microstructure contains unsintered accumulated Si and localized pores, which restricts its potential for engineering applications. The 40HS coating is optimized by reducing the Si content, which effectively mitigates the gradient differences in element distribution, significantly enhancing surface uniformity. This optimization decreases the porosity and increases the sintering density of the coating, significantly improving its surface uniformity and structural stability. Besides, the layered gradient structure effectively prevents the coating from cracking caused by CTE mismatch. The phase composition of each layer of the coating remains stable with reduced porosity and increased sintering density, demonstrating superior metallurgical bonding performance and structural stability.

It is noteworthy that experiment results verify the presence of unreacted metallic Hf in both coatings, indicating the relatively low kinetic rate of the Hf-Si reaction, which leads to complete conversion being challenging under current process conditions. Future research should introduce metal elements with higher reactivity with Si, such as Zr or Mo, to accelerate the formation of high-silicon phases, thereby forming a continuous and dense ceramic protective layer on the surface, and further enhancing the oxidation resistance and service life of the coating. Additionally, based on the potential synergistic protective mechanism of HfO_2/$Hf_6Ta_2O_{17}$-SiO_2 composite oxide films in the oxidized coating, further studies should combine thermodynamic simulations with dynamic oxidation experiments to deeply investigate the failure behavior and multiphase synergistic strengthening pathways of the coating under extreme environments, providing theoretical support for the composition design and performance tuning of high-temperature protective coatings.

5 Conclusions

1) To enhance the high-temperature oxidation resistance of Ta12W alloy, Hf-Ta-Si composite silicide coatings were prepared on the alloy surface using the slurry reactive sintering process. The as-prepared coating exhibits a multi-layer gradient structure: the upper layer primarily consists of refractory metal silicide HfSi and ultra-high-temperature ceramic particles HfC; the middle layer is dominated by Ta_5Si_3 solid solution with dissolved high-melting-point elements, such as Hf and W; the main layer is composed of the high-silicide phase $TaSi_2$; Ta_5Si_3 interface diffusion layer is at the bottom. The layered gradient structure effectively prevents the coating cracking caused by CTE mismatch.

2) The Hf:Si mass ratio can influence the surface uniformity of the coating from top to bottom. The 30HSi sample exhibits inferior surface uniformity due to its high Si content, resulting in the accumulation of unmelted Si at the bottom of the sample. The optimized 40HS sample has stable phase composition, which effectively mitigates the gradient differences in elemental distribution due to the reduced Si content. This optimization decreases the porosity and increases the sintering density of the coating, significantly improving its surface uniformity and structural stability.

3) During the preparation of Hf-Ta-Si composite coating, the acid-alcohol resin in the organic solvent undergoes high-temperature pyrolysis and in-situ reacts with Hf to form ultra-

high-temperature ceramic HfC, which is expected to enhance the oxidation resistance and high-temperature stability of coating.

4) The presence of unreacted metallic Hf in the coating indicates that the reaction kinetics of Hf-Si is relatively slow, leading to difficult complete conversion under current process conditions. Future research should introduce more reactive metals (such as Zr or Mo) to accelerate the formation of high-silicide phases, thereby forming a continuous and dense ceramic protective layer on the surface.

References

1 Obinna U, Najafi H. *Acta Astronautica*[J], 2020, 176: 341

2 Cai Zhenyang, Zhao Xiaojun, Zhang Daxu *et al*. *Corrosion Science*[J], 2018, 143: 116

3 Hua Nengbin, Wang Wenjie, Wang Qianting *et al*. *Journal of Alloys and Compounds*[J], 2021, 861: 157997

4 Cai Zhenyang, Wu Yonghuang, Liu Hunyun *et al*. *Materials & Design*[J], 2018, 155: 463

5 Cai Zhenyang, Zhang Daxu, Chen Xinxiang *et al*. *Journal of the European Ceramic Society*[J], 2019, 39(7): 2277

6 Li Shan, Xiao Lairong, Liu Sainan *et al*. *Journal of the European Ceramic Society*[J], 2022, 42(12): 4866

7 Xiao Lairong, Xu Xueqing, Liu Sainan *et al*. *Journal of the European Ceramic Society*[J], 2020, 40(10): 3555

8 Xu Jiawei, Xiao Lairong, Zhang Yafang *et al*. *Corrosion Science*[J], 2023, 224: 111563

9 Sun L, Fu Q G, Sun J. *Corrosion Science*[J], 2020, 176: 109051

10 Zhang Y, Fu T, Yu L *et al*. *Ceramics International*[J], 2022, 48(14): 20895

11 Zhang Y, Fu T, Zhu J *et al*. *Journal of Materials Research and Technology*[J], 2023, 24: 6076

12 Fu T, Zhang C, Zhang Y *et al*. *Materials Characterization*[J], 2025, 223: 114923

13 Fu T, Zhang Y, Chen L *et al*. *Journal of Materials Research and Technology*[J], 2024, 29: 491

14 Liu M, Hu L, Kang X *et al*. *Journal of Materials Science & Technology*[J], 2025, 225: 111

15 Lin D, Hu J, Wu R *et al*. *International Journal of Plasticity*[J], 2024, 183: 104142

16 Wang X, Zhang W, Wang T *et al*. *Corrosion Science*[J], 2025, 251: 112914

17 Ren Xuanru, Li Hejun, Fu Qiangang *et al*. *Composites Part B: Engineering*[J], 2014, 66: 174

18 Li Jiachen, Li Tao, Huang Chengjun *et al*. *Corrosion Science*[J], 2024, 228: 111795

19 Zhang Menglin, Ren Xuanru, Chu Hongao *et al*. *Corrosion Science*[J], 2020, 177: 108982

20 Kovaleva M, Goncharov I, Novikov V *et al*. *Materials Today: Proceedings*[J], 2022, 49: 1423

21 Wang Yalei, Xiong Xiang, Li Guodong *et al*. *Corrosion Science*[J], 2013, 66: 177

22 Tong Mingde, Chen Chunjin, Fu Qiangang *et al*. *Journal of the European Ceramic Society*[J], 2022, 42: 2586

23 Chen Sian, Hu Haifeng, Zhang Yudi *et al*. *Materials & Design*[J], 2013, 51: 19

24 Liu Jixuan, Kan Yanmei, Zhang Guojun. *Journal of the American Ceramic Society*[J], 2010, 93(4): 980

25 Liu Z T Y, Burton B P, Khare S V *et al*. *Journal of Physics: Condensed Matter*[J], 2017, 29: 035401

26 An Jing, Song Jinpeng, Liang Guoxing *et al*. *Materials*[J], 2017, 10(5): 461

27 Behzad Mehdikhani, Gholam Hossein Borhani, Saeed Reza Bakhshi *et al*. *Bulletin of Materials Science*[J], 2016, 39(1): 79

28 Bradford C S, Daniel B, Gregory B T. *Journal of Materials Research*[J], 2015, 30(19): 2949

29 Ren Xuanru, Li Hejun, Li Kezhi *et al*. *Journal of Alloys and Compounds*[J], 2015, 618: 390

30 Ren Xuanru, Li Hejun, Fu Qiangang *et al*. *Corrosion Science*[J], 2014, 87: 479

31 Kiryukhantsev-Korneev P V, Sytchenko A D, Potanin A Y *et al*. *Surface and Coatings Technology*[J], 2020, 403: 126373

32 Kiryukhantsev-Korneev P V, Sytchenko A D, Sviridova T A *et al*. *Surface and Coatings Technology*[J], 2022, 442: 128141

33 Tong M D, Chen C J, Fu Q G *et al*. *Journal of the European Ceramic Society*[J], 2022, 42(6): 2586

34 Guo H, Wang B Z, Li R F *et al*. *Corrosion Science*[J], 2025, 247: 112772

35 Zhang M L, Ren X R, Chu H G *et al*. *Corrosion Science*[J], 2020, 177: 108982

36 Feng G H, Li H J, Yang L *et al*. *Corrosion Science*[J], 2020, 170: 108649

37 Lakiza S M, Tyschenko J A, Lopato L M. *Journal of the European Ceramic Society*[J], 2011, 31(7): 1285

38 Yang Y, Perepezko J H, Zhang C. *Materials Chemistry & Physics*[J], 2017, 197: 154

39 Cheng Chunyu, Lv Tiantian, Song Bohao *et al*. *Surfaces and Interfaces*[J], 2024, 53: 105050

40 Li M, Xu Q Y, Wang L *et al*. *Key Engineering Materials*[J], 2011, 40: 459

41 Wang Xin, Li Zhengxian, Du Jihong *et al*. *Equipment Environmental Engineering*[J], 2016, 13(3): 1

42 Antoio Augusto, Erika Coaglia, Maria Ismenia *et al*. *Journal of Phase Equilibria and Diffusion*[J], 2015, 36(3): 209

43 Zhao J C, Bewlay B P, Jackson M R *et al*. *Journal of Phase Equilibria*[J], 2000, 21(1): 40

44 Gao Jiantao, Li Changrong, Guo Cuiping *et al*. *Journal of Physics: Conference Series*[J], 2018, 1074: 012074

45 Swati Sharma. *Materials*[J], 2018, 11(10): 1857

46 Xu X F, Li X Y, Zhang B. *Journal of Materials Science & Technology*[J], 2023, 134: 223

47 Soumitra Roy, Aloke Paul. *Philosophical Magazine*[J], 2012, 92(34): 4215

Si含量对Ta12W合金表面Hf-Ta-Si涂层原位反应生成机理的影响

韩承序[1,2]，刘艳明[1]，汪　欣[2]，杨　涛[2]，严　鹏[2]
(1. 西安石油大学 材料科学与工程学院，陕西 西安 710065)
(2. 西北有色金属研究院，陕西 西安 710016)

摘　要：采用浆料反应烧结方法在Ta12W合金表面制备了Hf-Ta-Si复合涂层，探究了Si含量对Hf-Ta-Si涂层原位形成机理的影响。结果表明，30Hf:70Si涂层表面均一性差，含有一定孔洞，试样上部的涂层呈现4层梯度结构：最表层以HfSi和HfC为主，中间层形成$(Ta, Hf)_5Si_3$固溶体，下层主体层为$TaSi_2$高硅相，涂层/基体界面层为Ta_5Si_3。但大量熔融Si在重力作用下导致下部涂层表面的Si富集。优化Hf:Si比例至40:60后，涂层表面的元素分布梯度差异降低，其表层仍以HfSi/HfC为主，但HfC析出更均匀；中间层$(Ta, Hf)_5Si_3$固溶体连续性增强；底层与涂层/基体界面过渡层未发生明显改变，整体形成更加致密的多层梯度结构，且涂层表面的均一性得到明显改善。此外，有机溶剂中的酸醇树脂通过高温热解与Hf原位反应生成的超高温陶瓷HfC，有望提高涂层的抗氧化性能和高温稳定性。

关键词：钽合金；Hf-Ta-Si涂层；原位生成机制；HfC；梯度结构

作者简介：韩承序，男，1996年生，硕士，西安石油大学材料科学与工程学院，陕西 西安 710065，E-mail：916890739@qq.com